Multicenter continuum-state approach to molecular-frame photoelectron angular distributions: From plane-wave to twisted photons

Jiahao Duan,[1] Maomao Gong,[1,2,*] Yongjun Cheng,[1] and Song Bin Zhang[1,†]
[1]*School of Physics and Information Technology, Shaanxi Normal University, Xi'an 710119, China*
[2]*Department of Modern Physics, University of Science and Technology of China, Hefei 230026, China*

(Received 15 December 2023; revised 15 April 2024; accepted 28 May 2024; published 13 June 2024)

Theoretical characterization of the photoionization mechanism in atoms and molecules necessitates a precise depiction of the ionization continuum. However, the accurate inclusion of the correlated electronic wave function at short range, particularly for intricate multicenter molecules, poses a significant challenge. In this study, we have devised a multicenter continuum-state approach by solving the coupled-channel Schrödinger equation. This approach enables the computation of molecular frame photoelectron angular distributions (MFPADs) induced by both plane-wave and twisted photons. To elucidate our methodology, we present calculations focusing on the CO_2 C 1s orbital. Our computations exhibit favorable agreements with experimental observations and established theoretical frameworks for plane-wave photoionization. For the twisted-photon ionization, the MFPADs demonstrate independence from the orbital angular momentum (OAM) of the twisted light, provided no restrictions are imposed on the impact parameters. The MFPADs exhibit varying dependence on the opening angle for varying propagation directions of twisted photons, when considering linearly polarized vectors lying within the cone surface. Additionally, for a comprehensive comprehension of the OAM-dependent photoionization process, we investigate the MFPADs resulting from placing the molecule at the phase singularity in the twisted center.

DOI: 10.1103/PhysRevA.109.063114

I. INTRODUCTION

The developments of x-ray free-electron lasers (XFELs) delivering extremely short x-ray pulses of a few femtoseconds [1–4] have paved new pathways to image structural changes of molecules in chemical reactions, for example, employing time-resolved x-ray diffraction [5] and ultrafast electron diffraction [6]. Molecular frame photoelectron angular distribution, containing the most detailed information of molecular structure and photoionization dynamics, refers to the angular distribution of photoelectrons emitted from molecules in their own reference frame upon interaction with photons and has been used as a fundamental tool to investigate the relevant dynamics.

In molecular frame photoelectron angular distribution (MFPAD) experiments, molecules are aligned or oriented [7,8] in a specific manner before being irradiated with high-energy photons, such as x-rays or ultraviolet light. Alternatively, the orientation of the molecule can be determined by detecting the photoelectron in coincidence with charged fragments [9]. This approach is typically employed after core-level photoionization, where the dissociation occurs simultaneously with prompt Auger decay [10].

In the theoretical aspect, during the past few decades, numerous theoretical methods have been developed to address the issue. Since the pioneering works [11,12], various theoretical models, including the UK molecular R-matrix method [13,14], the complex Kohn method [15–17], the multiple scattering method [18], the ePolyScat method [19,20], the multichannel Schwinger configuration interaction method [21–23], and most recently, the XCHEM method [24–28], have been developed to compute the photon ionization cross sections. However, due to the complicated short-range structure of the correlated electronic wave functions, it is still a challenge to determine accurate representation of the ionization continuum state, especially for complex multicenter molecules. There is a long history of investigation of the plane wave photon ionization, as mentioned above. However, related research on twisted light is quite lagging. Matula *et al*. [29] investigated the angular distribution of emitted electrons from hydrogen-like ions by twisted photons, with special attention to the dependence of the electron emission pattern on the impact parameter of the ion with respect to the center of the twisted wave front. Then, in 2015, ionization of H_2^+ molecular ions by twisted Bessel light [30] was investigated with a simple plane-wave description of the ionized electron. Most recently, the photoelectron angular distributions generated by twisted radiation on atoms are investigated from a theoretical perspective [31], with special emphasis on the dipole and nondipole effects.

In the present work, a multicenter continuum-state approach is developed to describe the MFPAD induced by plane-wave and twisted photons by considering the photoelectron moving in the multicenter model potential. The multicenter continuum state is actually the solutions of the corresponding coupled-channel Schrödinger equation. The target electronic structure is constructed by means of single-center expansion based on the symmetry-adapted spherical harmonics [32–34]. The advantage of the present approach to MFPAD is that it is easy to extend to more complex

*Contact author: gongmm@snnu.edu.cn
†Contact author: song-bin.zhang@snnu.edu.cn

polyelectronic atoms and molecules with sufficient accuracy. As a demonstration, MFPADs for C 1s photoelectrons from CO_2 molecules are presented for the energies of ejected electron covering from several to 150 eV. Our computations exhibit favorable agreement with experimental observations and established theoretical frameworks for plane-wave photoionization. Furthermore, the MFPADs induced by twisted photons demonstrate independence from the OAM of the twisted light, provided no restrictions are imposed on the impact parameters. The MFPAD exhibits varying dependence on the opening angle for varying propagation directions of twisted photons, when considering linearly polarized vectors lie in a cone surface. Additionally, for a comprehensive comprehension of the OAM-dependent photoionization process, we investigate the MFPADs resulting from placing the molecule in the phase singularity in the twisted center.

The paper is organized as follows: in the next section we briefly outline the theoretical method for plane-wave and twisted photoionization. The results and discussion will be presented in Sec. III, followed by the summary in Sec. IV. Atomic units are used throughout the paper unless explicitly stated otherwise.

II. THEORETICAL METHODS

A. General form of molecular frame photoelectron angular distribution

1. Plane-wave photons

The core physics of MFPADs has been covered extensively in the literature; here, only a brief introduction is provided with sufficient detail to introduce the reconstruction of MFPAD. In the nonrelativistic region, for a plane-wave photon with wave vector $\boldsymbol{k}$, energy $\omega = k/\alpha$, the transition operator reads

$$\hat{V}^{(\mathrm{pl})} = \alpha \boldsymbol{A}_{\lambda}^{(\mathrm{pl})}(\boldsymbol{r}) \cdot \hat{\boldsymbol{p}}, \tag{1}$$

where α is fine-structure constant, $\hat{\boldsymbol{p}} = -i\nabla$ is the linear momentum operator, and the vector potential is expressed as

$$\boldsymbol{A}_{\lambda}^{(\mathrm{pl})}(\boldsymbol{r}) = \boldsymbol{e}_{k\lambda} e^{i\boldsymbol{k}\cdot\boldsymbol{r}}, \tag{2}$$

where $\boldsymbol{e}_{k\lambda}$ denotes the polarization vector with $\lambda = \pm 1$, and λ is associated with helicity of the incident wave. Then, the photoionization differential cross section [35] with plane-wave photon is

$$\frac{d^2\sigma^{(\mathrm{pl})}}{d\Omega d\hat{k}} = \frac{2\pi}{j^{\mathrm{pl}}} n_i \left| \langle \mathcal{F}_{\boldsymbol{k}_e}^{(-)}(\boldsymbol{r}) | \alpha e^{i\boldsymbol{k}\cdot\boldsymbol{r}} \boldsymbol{e}_{k\lambda} \cdot \hat{\boldsymbol{p}} | \varphi_i(\boldsymbol{r}) \rangle \right|^2, \tag{3}$$

where $j^{\mathrm{pl}} = k/(2\pi)$ is the flux of the incident plane photon radiation [36], n_i denotes the occupation number of the ionized orbital, then

$$\frac{d^2\sigma^{(\mathrm{pl})}}{d\Omega d\hat{\boldsymbol{k}}} = \frac{4\pi^2 \alpha n_i}{\omega} \left| M_{fi}^{(\mathrm{pl})}(\boldsymbol{k}) \right|^2, \tag{4}$$

and $M_{fi}^{(\mathrm{pl})}(\boldsymbol{k})$ is the plane-wave transition amplitude,

$$M_{fi}^{(\mathrm{pl})}(\boldsymbol{k}) = \langle \mathcal{F}_{\boldsymbol{k}_e}^{(-)}(\boldsymbol{r}) | e^{i\boldsymbol{k}\cdot\boldsymbol{r}} \boldsymbol{e}_{k\lambda} \cdot \hat{\boldsymbol{p}} | \varphi_i(\boldsymbol{r}) \rangle; \tag{5}$$

Ω defines the molecular orientation with respect to the laboratory frame, and $\boldsymbol{k}_e$ is the momentum vector of the ionized electron. $\varphi_i(\boldsymbol{r})$ and $\mathcal{F}_{\boldsymbol{k}_e}^{(-)}(\boldsymbol{r})$ are the initial bound and final multicenter continuum states of the active electron, respectively. In the dipole approximation, $e^{i\boldsymbol{k}\cdot\boldsymbol{r}} \approx 1$, then Eq.(4) can be simplified to the usually adopted formula in the length form [35,37]

$$\frac{d^2\sigma^{(\mathrm{pl})}}{d\Omega d\hat{\boldsymbol{k}}} = 4\pi^2 \alpha \omega n_i \left| \langle \mathcal{F}_{\boldsymbol{k}_e}^{(-)}(\boldsymbol{r}) | \boldsymbol{e}_{k\lambda} \cdot \boldsymbol{r} | \varphi_i(\boldsymbol{r}) \rangle \right|^2. \tag{6}$$

$\lambda = 1$ and -1 correspond to the right and left circular light, respectively, with propagation direction along the z axis. For linear polarized light, the vector potential can be denoted as

$$\begin{aligned} A_x^{(\mathrm{pl})}(\boldsymbol{r}) &= \frac{1}{\sqrt{2}} \left[A_{\lambda=1}^{(\mathrm{pl})}(\boldsymbol{r}) + A_{\lambda=-1}^{(\mathrm{pl})}(\boldsymbol{r}) \right], \\ A_y^{(\mathrm{pl})}(\boldsymbol{r}) &= \frac{i}{\sqrt{2}} \left[A_{\lambda=1}^{(\mathrm{pl})}(\boldsymbol{r}) - A_{\lambda=-1}^{(\mathrm{pl})}(\boldsymbol{r}) \right], \end{aligned} \tag{7}$$

with a linearly polarized vector along the x and y axis, respectively. Then, the transition amplitude induced by linearly polarized light can be composed of a superposition of the transition amplitudes of right and left circular polarized light.

In the present work, we consider ionization induced by linearly polarized photons, as shown in Fig. 1. In order to calculate the transition amplitude, the bound and the final multicenter continuum state are expanded on the symmetry-adapted angular function $X_{h\ell}^{p\mu}(\theta, \phi)$ [32–34] by utilizing the point-group symmetry of the molecule, where p and μ label one of the relevant irreducible representations and one of its components, respectively. The bound wave functions of the molecular orbitals (MOs) are calculated using the GAUSSIAN09 [38] program with the density functional theory employing the B3LYP functional [39,40] and cc-pVTZ [41] basis set. The numerical processes for the transition amplitude in length and velocity forms are presented in Appendix B.

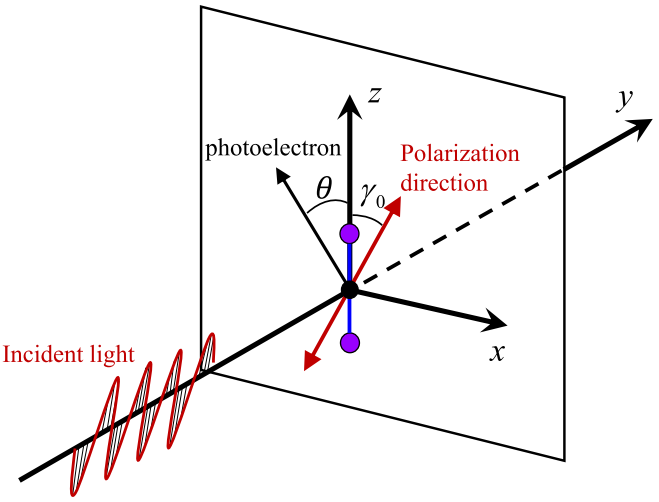

FIG. 1. The schematic of photoionization process induced by linearly polarized plane-wave photons, with propagation direction along y-axis.

2. Twisted photons

In order to describe the twisted-photon ionization process, the spatial part of the vector potential in the transition

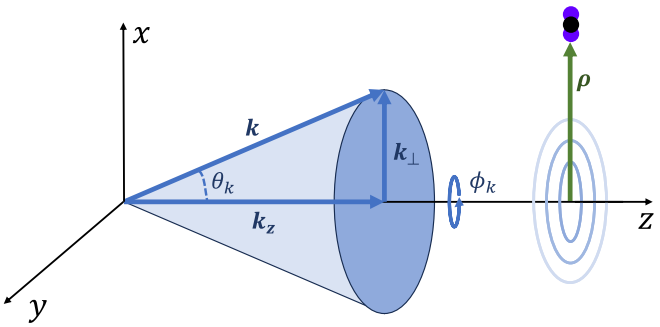

FIG. 2. Overview of the twist light incidents on a molecular target with impact parameter $\boldsymbol{\rho}$.

operator [Eq.(1)] should be changed from plane wave to twisted wave. Twisted photons with intrinsic OAM $m_\gamma\hbar$ and energy ε can be described in the cylindrical coordinates $\boldsymbol{r} = (\boldsymbol{r}_\perp, z) = (r_\perp, \phi_r, z)$. The momentum vector of twisted photon is defined as $\boldsymbol{k} = (\boldsymbol{k}_\perp, k_z) = (k_\perp, \phi_k, k_z)$, which lays on the surface of a cone with an opening angle $\theta_k = \arctan(|\boldsymbol{k}_\perp|/\mathrm{k_z}) = \arctan(\kappa/\mathrm{k_z})$. ϕ_k is defined as the rotation angle. In the present work, we adopt the Bessel state description of twisted photons; in the real space, it is expressed as [36,42,43]

$$\langle \boldsymbol{r} \mid k_z \kappa m_\gamma \rangle = e^{ik_z z} \psi_{\mathrm{tr}}^{\kappa m_\gamma}(\boldsymbol{r}_\perp), \tag{8}$$

and the transverse component of the wave function equals to

$$\psi_{\mathrm{tr}}^{\kappa m_\gamma}(\boldsymbol{r}_\perp) = \sqrt{\kappa}\frac{e^{im_\gamma\phi_r}}{\sqrt{2\pi}} J_{m_\gamma}(\kappa r_\perp), \tag{9}$$

where $J_{m_\gamma}(\kappa r_\perp)$ is the m_γth Bessel function of the first kind. The momentum representation of the stationary Bessel solution is

$$\begin{aligned}\psi_{\mathrm{tr}}^{\kappa m_\gamma}(\boldsymbol{k}_\perp) &= \int \frac{e^{im_\gamma\phi_r}}{\sqrt{2\pi}}\sqrt{\kappa} J_{m_\gamma}(\kappa r_\perp) e^{-i\boldsymbol{k}_\perp\cdot\boldsymbol{r}_\perp} d\boldsymbol{r}_\perp \\ &= (-i)^{m_\gamma} e^{im_\gamma\phi_k}\sqrt{\frac{2\pi}{k_\perp}}\delta(k_\perp - \kappa).\end{aligned} \tag{10}$$

So, the Bessel state of Eq. (8) can be written as

$$\begin{aligned}\langle \boldsymbol{r} \mid k_z \kappa m_\gamma \rangle &= e^{ik_z z}\int \psi_{\mathrm{tr}}^{\kappa m_\gamma}(\boldsymbol{k}_\perp) e^{i\boldsymbol{k}_\perp\cdot\boldsymbol{r}_\perp}\frac{d\boldsymbol{k}_\perp}{(2\pi)^2} \\ &= (-i)^{m_\gamma}\sqrt{\frac{\kappa}{2\pi}}\int_0^{2\pi} e^{im_\gamma\phi_k} e^{i\boldsymbol{k}\cdot\boldsymbol{r}}\frac{d\phi_k}{2\pi}.\end{aligned} \tag{11}$$

Then, a Bessel state of light is characterized by the vector potential [36,42,43]

$$\begin{aligned}\boldsymbol{A}^{(\mathrm{tw})}_{k_z\kappa m_\gamma\lambda}(\boldsymbol{r},\boldsymbol{\rho}) &= e^{ik_z z}\int \boldsymbol{e}_{\boldsymbol{k}\lambda}\psi_{\mathrm{tr}}^{\kappa m_\gamma}(\boldsymbol{k}_\perp) e^{i\boldsymbol{k}_\perp\cdot\boldsymbol{r}_\perp}\frac{d\boldsymbol{k}_\perp}{(2\pi)^2} \\ &= (-i)^{m_\gamma}\sqrt{\frac{\kappa}{2\pi}}\int_0^{2\pi}\boldsymbol{e}_{\boldsymbol{k}\lambda} e^{im_\gamma\phi_k - i\boldsymbol{k}\cdot\boldsymbol{\rho}} e^{i\boldsymbol{k}\cdot\boldsymbol{r}}\frac{d\phi_k}{2\pi},\end{aligned} \tag{12}$$

where the exponential term $e^{-i\boldsymbol{k}\cdot\boldsymbol{\rho}}$ specifies the displacements of the twisted photons relative to the molecular target, and $\boldsymbol{\rho}$ is defined as impact parameters, as shown in Fig. 2. As can be seen from these expressions, such a Bessel beam can be understood as a superposition of plane waves whose wave vectors

$$\boldsymbol{k} = \begin{pmatrix} k\sin\theta_k\cos\phi_k \\ k\sin\theta_k\sin\phi_k \\ k\cos\theta_k \end{pmatrix} \tag{13}$$

form the surface of a cone and with the polarization vectors [29,30]

$$\boldsymbol{e}_{\boldsymbol{k}\lambda} = \frac{-\lambda}{\sqrt{2}}\begin{pmatrix} \cos\theta_k\cos\phi_k - i\lambda\sin\phi_k \\ \cos\theta_k\sin\phi_k + i\lambda\cos\phi_k \\ -\sin\theta_k \end{pmatrix}. \tag{14}$$

Combining Eqs. (12) and (5), the transition amplitude for the twisted photon is expressed as

$$M^{(\mathrm{tw})}_{fi}(\boldsymbol{k},\boldsymbol{\rho}) = (-i)^{m_\gamma}\sqrt{\frac{\kappa}{2\pi}}\int_0^{2\pi} e^{im_\gamma\phi_k - i\boldsymbol{k}\cdot\boldsymbol{\rho}} M^{(\mathrm{pl})}_{fi}(\boldsymbol{k})\frac{d\phi_k}{2\pi}. \tag{15}$$

In the practice, the impact parameter $\boldsymbol{\rho}$ is usually not available, as a macroscopic target of an atom or molecule is assumed to be randomly distributed over the extent of the incident twisted light beam in a large radius R. In the theoretical aspect, we must integrate the impact parameters of cross sections to achieve agreement with the experiment. Therefore, by integrating $|M^{(\mathrm{tw})}_{fi}(\boldsymbol{k},\boldsymbol{\rho})|^2$ over all the impact parameter $\boldsymbol{\rho}$ in the transverse plane in a large radius R, the photoionization differential cross section induced by twisted photons can be determined:

$$\begin{aligned}\frac{d^2\sigma^{(\mathrm{tw})}}{d\Omega d\hat{\boldsymbol{k}}} &= \frac{2\pi\alpha^2 n_i}{j^{\mathrm{tw}}}\int_{0<|\boldsymbol{\rho}|<R}\frac{d\boldsymbol{\rho}}{\pi R^2}\left|M^{(\mathrm{tw})}_{fi}(\boldsymbol{k},\boldsymbol{\rho})\right|^2 \\ &= \frac{2\pi\alpha^2 n_i}{j^{\mathrm{tw}}}\frac{2\pi}{\kappa}\int_{0<|\boldsymbol{\rho}|<R}\frac{d\boldsymbol{\rho}}{\pi R^2} \\ &\quad\times\int e^{im_\gamma\phi_k}\delta(\kappa - k_\perp)M^{(\mathrm{pl})}_{fi}(\boldsymbol{k}) e^{-i\boldsymbol{\rho}\cdot\boldsymbol{k}_\perp}\frac{d\boldsymbol{k}_\perp}{(2\pi)^2} \\ &\quad\times\int e^{-im_\gamma\phi_{k'}}\delta(\kappa - k'_\perp)M^{(\mathrm{pl})*}_{fi}(\boldsymbol{k}') e^{i\boldsymbol{\rho}\cdot\boldsymbol{k}'_\perp}\frac{d\boldsymbol{k}'_\perp}{(2\pi)^2},\end{aligned} \tag{16}$$

where $j^{\mathrm{tw}} = k\cos\theta_k/(2\pi^3 R)$ denotes the flux of the incident twisted-photon radiation [36]. With the help of the following integral,

$$\int_{0<|\boldsymbol{\rho}|<\infty} d^2\rho e^{i\boldsymbol{\rho}\cdot(\boldsymbol{p}''-\boldsymbol{p}')} = (2\pi)^2\delta_2(\boldsymbol{p}'_\perp - \boldsymbol{p}''_\perp), \tag{17}$$

for a large R ($R\to\infty$), Eq.(16) can be simplified by integrating $d\boldsymbol{\rho}$ and $d\boldsymbol{k}'_\perp$,

$$\begin{aligned}&\int_{0<|\boldsymbol{\rho}|<R}\frac{d\boldsymbol{\rho}}{\pi R^2}\left|M^{(\mathrm{tw})}_{fi}(\boldsymbol{k},\boldsymbol{\rho})\right|^2 \\ &\quad= \frac{1}{2\pi\kappa}\frac{1}{\pi R^2}\int\left|\delta(\kappa - k_\perp)M^{(\mathrm{pl})}_{fi}(\boldsymbol{k})\right|^2 d\boldsymbol{k}_\perp.\end{aligned} \tag{18}$$

Then, by using the expression of the delta function squared fromRefs. [36,44],

$$\delta^2(k_\perp - \kappa) = \frac{R}{\pi}\delta(k_\perp - \kappa), \tag{19}$$

and performing the integration over $k_\perp$, finally, the twisted-photon-induced differential cross section yields

$$\frac{d^2\sigma^{(\mathrm{tw})}}{d\Omega d\hat{\boldsymbol{k}}} = \frac{4\pi^2\alpha n_i}{\omega\cos\theta_\mathrm{k}}\int \left|M_{fi}^{(\mathrm{pl})}(\boldsymbol{k})\right|^2 \frac{d\phi_k}{2\pi}. \tag{20}$$

The equation shows that twisted-photon-induced photoionization cross sections do not depend on the OAM of twisted photons, provided that no restrictions are imposed on the impact parameters. We here note that if the opening angle $\theta_k = 0^\circ$, the expression of Eq. (20) will simply degenerate into formulation of the photoionization differential cross section induced by plane-wave photons.

B. Multicenter continuum state

In order to obtain the multicenter continuum state, the photoelectron is regarded as moving in the anisotropic field of the residual ion. In this work, a model potential is adopted [45]:

$$V^\mathrm{m} = V^\mathrm{st} + V^\mathrm{cp} + V^\mathrm{ex}, \tag{21}$$

where V^st is the electrostatic potential between the electron and residual molecular ion. V^cp is the correlation-polarization potential [34,45,46]. V^ex is the free electron gas (FEGE) model exchange potential [34,45,46].

In the molecular coordinate, the multicenter continuum orbital based on the single active electron approximation for particular irreducible representations and its component $p\mu$ satisfies the following Schrödinger equation:

$$\left[-\tfrac{1}{2}\nabla^2 + V^m - E_{k_e}\right]F^{p\mu}(\boldsymbol{r}) = 0. \tag{22}$$

The multicenter continuum orbital $F^{p\mu}(\boldsymbol{r})$ is expanded on the symmetry-adapted angular function $X_{h\ell}^{p\mu}(\hat{\boldsymbol{r}})$ [32–34]:

$$F^{p\mu}(\boldsymbol{r}) = \sum_{h'\ell'}\frac{1}{r}f_{h'\ell'}^{p\mu}(r)X_{h'\ell'}^{p\mu}(\hat{\boldsymbol{r}}); \tag{23}$$

insert the formula into the Schrödinger equation and project on $X_{h'l'}^{p\mu}(\hat{\boldsymbol{r}})$ by utilizing its normalization relationship,

$$\left[\frac{d^2}{dr^2} - \frac{\ell(\ell+1)}{r^2} + \frac{2}{r} + k_e^2\right]f_{h\ell}^{p\mu}(k_e, r) = \sum_{h'\ell'}U_{h\ell;h'\ell'}^{p\mu}(k_e, r)f_{h'\ell'}^{p\mu}(k_e, r), \tag{24}$$

where the potential matrix element is

$$U_{h\ell,h'\ell'}^{p\mu}(k_e, r) = 2\left\langle X_{h\ell}^{p\mu}(\hat{\boldsymbol{r}})\left|V^m(k_e, \boldsymbol{r})\right|X_{h'\ell'}^{p\mu}(\hat{\boldsymbol{r}})\right\rangle + \frac{2}{r}\delta_{hh'}\delta_{\ell\ell'}. \tag{25}$$

The multicenter model potential V^m leads to the coupling for different angular momentum. In general, if a cutoff of N terms for the maximum of angular momentum ℓ is applied, there are N independent solutions for the N differential equations. Therefore, the multicenter continuum orbital consists of N independent solutions:

$$F_{h''\ell''}^{p\mu}(\boldsymbol{r}) = \sum_{h\ell}\frac{1}{r}f_{h\ell,h''\ell''}^{p\mu}(r)X_{h\ell}^{p\mu}(\hat{\boldsymbol{r}}), \tag{26}$$

which leads to the following coupled equations:

$$\left[\frac{d^2}{dr^2} - \frac{\ell''(\ell''+1)}{r^2} + \frac{2}{r} + k_e^2\right]f_{h\ell;h''\ell''}^{p\mu}(k_e, r) = \sum_{h'\ell'}U_{h\ell;h'\ell'}^{p\mu}(k_e, r)f_{h'\ell';h''\ell''}^{p\mu}(k_e, r), \tag{27}$$

The coupled equations are further solved by an improved log-derivative method [47], and the detailed numerical processes are displayed in Appendix A. In order to solve the equation, the radial wave functions $f_{h\ell;h''\ell''}^{p\mu}$ must match the physical asymptotic conditions of the $\mathcal{K}$ matrix [48]:

$$\begin{aligned} f_{h\ell;h'\ell'}^{p\mu}(k_e, r) &\overset{r\to 0}{\to} \mathcal{N}_\ell r^{\ell+1}\delta_{h\ell;h'\ell'} \\ f_{h\ell;h'\ell'}^{p\mu}(k_e, r) &\overset{r\to\infty}{\to} F_\ell(k_e r)\delta_{h\ell;h'\ell'} + G_\ell(k_e r)\mathcal{K}_{h\ell;h'\ell'}^{p\mu}, \end{aligned} \tag{28}$$

where F_ℓ and G_ℓ are the regular and irregular Coulomb functions.

The multicenter continuum wave function for momentum $\boldsymbol{k}$ is the linear combination of the multicenter continuum orbitals:

$$\mathcal{F}_{\boldsymbol{k}_e}^{(-)}(\boldsymbol{r}) = \sum_{p\mu;h''\ell''}F_{h''\ell''}^{p\mu}(\boldsymbol{r})a_{h''\ell''}^{p\mu}. \tag{29}$$

In order to obtain the coefficient $a_{h''\ell''}^{p\mu}$, we have to inspect the physical asymptotic conditions at $r \to \infty$. By utilizing Eq. (28) and F_ℓ and G_ℓ at $r \to \infty$,

$$\begin{aligned} \mathcal{F}_{\boldsymbol{k}_e}^{(-)}(\boldsymbol{r}) &\overset{r\to\infty}{\to} \sum_{p\mu;h''\ell''}\frac{1}{r}\left[\sin\theta_l\delta_{h\ell;h''\ell''} + \cos\theta_\ell\mathcal{K}_{h\ell;h''\ell''}^{p\mu}\right]a_{h''\ell''}^{p\mu}X_{h\ell}^{p\mu}(\hat{\boldsymbol{r}}) \\ &= \sum_{p\mu;h''\ell''}\frac{1}{r}\left[e^{i\theta_\ell}\frac{1}{2i}\left(\delta_{hl;h''\ell''} + i\mathcal{K}_{h\ell;h''\ell''}^{p\mu}\right) + e^{-i\theta_\ell}\frac{-1}{2i}\left(\delta_{h\ell;h''\ell''} - iK_{h\ell;h''\ell''}^{p\mu}\right)\right]a_{h''\ell''}^{p\mu}X_{h\ell}^{p\mu}(\hat{\boldsymbol{r}}), \end{aligned} \tag{30}$$

where $\theta_l = k_e r - \frac{l\pi}{2} + \sigma_l - \eta \ln 2k_e r$, $\eta = z/k_e$, $\sigma_l = \arg\Gamma(l+1+i\eta)$ is the Coulomb phase shift. Here, $\mathcal{F}_k^{(-)}(\boldsymbol{k_e}, \boldsymbol{r})$ satisfies the ingoing boundary condition. Let $\varphi_c^{(-)}(\boldsymbol{k_e}, \boldsymbol{r})$ denote the continuum wave function of electrons in the Coulomb potential and satisfy the ingoing boundary condition, then

$$\varphi_c^{(-)}(\boldsymbol{k_e}, \boldsymbol{r}) \overset{r\to\infty}{\to} \frac{1}{(2\pi)^{\frac{3}{2}}} \sum_{p\mu} \sum_{h\ell} 4\pi i^{-\ell} e^{i\sigma_\ell} \frac{1}{k_e r} F_\ell(k_e, r) X_{h\ell}^{p\mu}(\hat{\boldsymbol{k}}_{\boldsymbol{e}}) X_{h\ell}^{p\mu}(\hat{\boldsymbol{r}})$$
$$= \frac{1}{(2\pi)^{\frac{3}{2}}} \sum_{p\mu} \sum_{h\ell} 4\pi i^{-\ell} e^{i\sigma_\ell} \frac{1}{k_e r} \left[e^{i\theta_\ell} \frac{1}{2i} + e^{-i\theta_\ell} \frac{-1}{2i} \right] X_{h\ell}^{p\mu}(\hat{\boldsymbol{k}}_{\boldsymbol{e}}) X_{h\ell}^{p\mu}(\hat{\boldsymbol{r}}). \tag{31}$$

The coefficient $a_{h''\ell''}^{p\mu}$ can be determined by setting the same of the the outgoing spherical part of Eqs. (30) and (31),

$$a_{h''\ell''}^{p\mu} = \frac{1}{(2\pi)^{\frac{3}{2}}} \frac{4\pi}{k_e} \sum_{h'\ell'} ([\mathcal{I} + i\mathcal{K}^{p\mu}]^{-1})_{h''\ell'';h'\ell'} \times i^{\ell'} e^{-i\sigma_{\ell'}} X_{h'\ell'}^{p\mu}(\hat{\boldsymbol{k}}_{\boldsymbol{e}}). \tag{32}$$

So, the multicenter continuum wave function of the photoelectron can be expressed as

$$\mathcal{F}_{\boldsymbol{k_e}}^{(-)}(\boldsymbol{r}) = \frac{1}{(2\pi)^{\frac{3}{2}}} \sum_{p\mu} \sum_{h_1\ell_1;h_2\ell_2} 4\pi i^{-\ell_1} e^{i\sigma_{\ell_1}} \frac{1}{k_e r} \times \phi_{h_1\ell_1;h_2\ell_2}^{p\mu}(k_e, r) X_{h_1\ell_1}^{p\mu}(\hat{\boldsymbol{k}}_{\boldsymbol{e}}) X_{h_2\ell_2}^{p\mu}(\hat{\boldsymbol{r}}) \tag{33}$$

and

$$\phi_{h_1\ell_1;h_2\ell_2}^{p\mu}(k_e, r) = \sum_{h\ell} f_{h_1\ell_1;h\ell}^{p\mu}(k_e, r) ([\mathcal{I} + i\mathcal{K}^{p\mu}]^{-1})_{h\ell;h_2\ell_2}; \tag{34}$$

the short-range phase shift is included in the expression of Eq. (34).

III. RESULTS AND DISCUSSION

In order to evaluate the validity of the present model, for plane-wave photoionization, MFPADs for C 1s photoelectrons from CO_2 molecules are presented for the energies of ejected electron covering from several to 150 eV. Our computations exhibit favorable agreements with experimental observations and established theoretical frameworks. For the twisted-photon ionization, the MFPADs show independence from the OAM of the twisted light, as long as no restrictions are placed on the impact parameters. This finding highlights the unique features of MFPADs across different propagation directions of twisted photons, when considering linearly polarized vectors lying within a cone surface. Furthermore, to fully understand the OAM-dependent photoionization process, we examine the MFPADs generated when the molecule is positioned in the phase singularity at the twisted center. In the practical calculations, the equilibrium geometry of CO_2 possesses a $D_{\infty h}$ point group with a bond length of $R_{CO} = 1.163$ Å. To ensure the convergence for the numerical calculations, in the practical calculations, the upper limit of the partial wave expansion for the multicenter photoelectron continuum state is $l_{\text{cmax}} = 18$, while the upper limit of the initial bound state of the C 1s orbital is $l_{\text{bmax}} = 10$.

A. Plane-wave photons

Figure 3 shows the two-dimensional (2D) density plots of MFPADs for C 1s from CO_2 molecules with ejected electron energies of $E_e = 6.2$, 9.4, 14.6, 23.3, and 32.2 eV (corresponding to photon energies of 303.8 eV, 307 eV, 312.2 eV, 320.9 eV, and 329.8 eV, the C 1s ionization energy is 297.63 eV [49]), obtained by the present calculations. γ_0 (x axis) is defined as the angle between the molecular orientation and polarization of photons, and θ_e is the direction of photoelectrons emitted from the fixed molecule. For the equilibrium linear CO_2 molecule, due to the molecular symmetry, the distribution of photoelectrons exhibits isotropy for azimuthal angle ϕ_e, which will not be presented as a variable. The calculated MFPADs in Fig. 3 are in agreement with the calculations and the experimental data reported by Liu *et al*. [50], which are not displayed in the present work. Experimentally [51], the shape resonance located at approximately 14.6 eV is assigned to the promotion of an electron from the $2\sigma_g$ (C 1s) core orbital to the $4\sigma_u$ unoccupied molecular orbital. As a result, the final state can be described as $2\sigma_g^{-1}(^2\Sigma_g^+)4\sigma_u{}^1\Sigma_u$. This photoexcitation from $\Sigma_g \to \Sigma_u$ represents a parallel transition, where the ejected electron predominantly exhibits σ_u symmetry. In Fig. 3, $\gamma_0 = 0^\circ$ and 90° correspond to parallel ($\Sigma \to \Sigma$) and perpendicular ($\Sigma \to \Pi$) transitions, respectively. For the other polarization direction, such as γ_0 equal to 45°, it is actually the mixtures of $\Sigma \to \Sigma$ and $\Sigma \to \Pi$ transitions. The observed electron emission at approximately 14.6 eV mainly occurs at $\gamma_0 = 0^\circ$, aligned along the molecular axis. With the increasing of ejected electron energy from 14.6 eV to 23.3 eV, most of the photoelectrons come from the parallel transition, with a nodal plane at $\gamma_0 = 90^\circ$ in this energy region. For the ejected electron energy of 32.2 eV, the perpendicular transition is strongly enhanced, as shown in Fig. 3(e). These findings are consistent with the expectation that the shape resonance represents a parallel Σ_g to Σ_u transition, emitting photoelectrons with σ_u symmetry. These results additionally serve as evidence of the accuracy of the current calculations. At equilibrium geometry, the MFPAD for the parallel transition, i.e., $\gamma_0 = 0^\circ$, will always possess symmetric distribution relative to the center in the calculations. The experimental data reported by Liu *et al*. [50] exhibits asymmetric shapes except for $E_e = 32.17$ eV, as shown in Fig. 4. Our calculations of MFPADs at equilibrium and asymmetric geometries are also presented for comparison. The asymmetric geometry is adopted at CO distances of 1.136 and 1.193 Å, respectively, which are determined by the root-mean-square displacements in the harmonic asymmetric-stretch potential and were derived by Miyabe [16] from a normal mode analysis of the

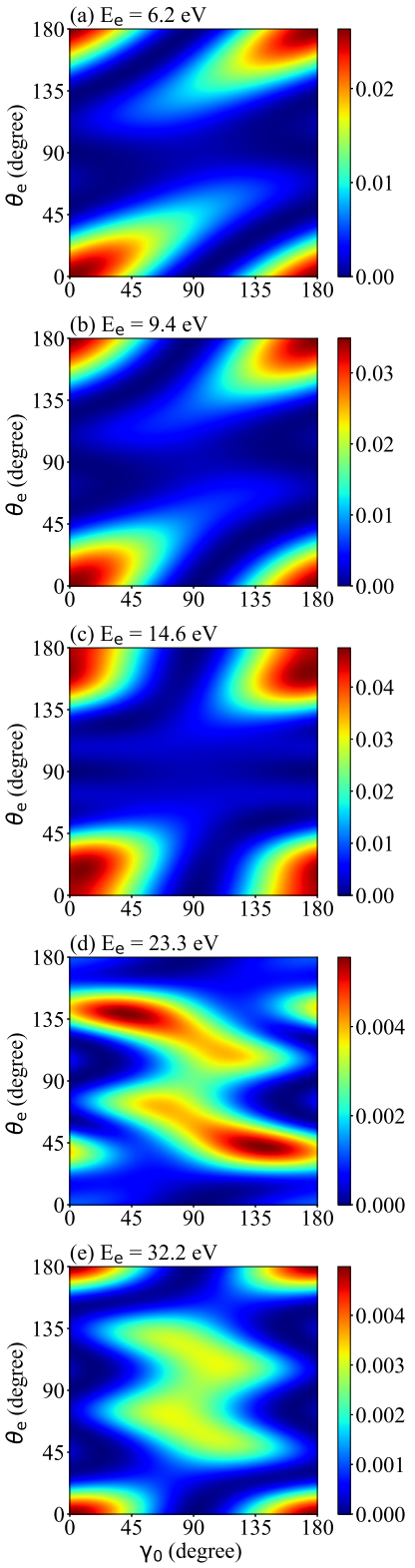

FIG. 3. 2D plots of MFPADs for C 1s photoelectrons from CO_2 molecules at $E_e = 6.2$, 9.4, 14.6, 23.3, and 32.2 eV. γ_0 is defined as the angle between the molecular orientation and polarization of photons.

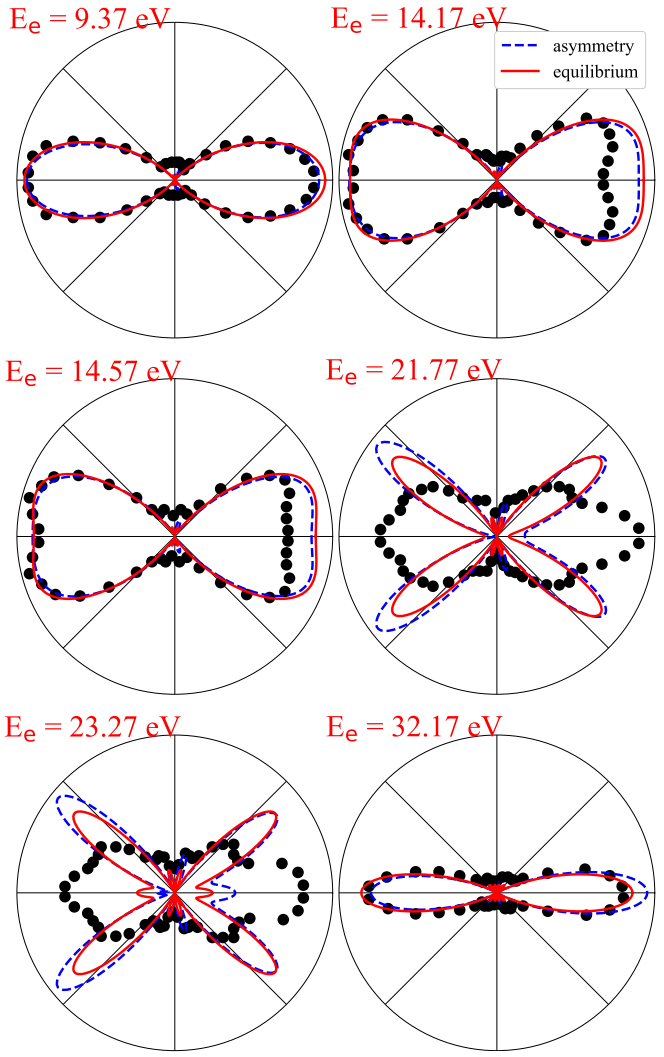

FIG. 4. Polar plots of C 1s MFPADs of CO_2 with molecular orientation parallel to the $\hat{\boldsymbol{e}}$ vector at photoelectron energies 9.37, 14.17, 14.57, 21.77, 23.27, and 32.17 eV. The dots correspond to measurements reported in Ref. [50]. Solid red and dashed blue curves are present calculations with equilibrium ($R_{CO} = 1.136$ Å) and asymmetric (CO distances are 1.136 and 1.193 Å) geometries, respectively.

ground-state CO_2 potential calculated at the MP2 level with a triple-zeta plus polarization basis. It shows that the asymmetry is clearly evident in MFPADs. Present calculations for the asymmetric geometries (dashed blue lines) are in excellent agreement with the calculations by Miyabe [16], and are in better agreement with the measurements at $E_e = 14.17$ and 14.57 eV. However, the disagreement between the measured and calculated spectra at $E_e \sim 20$ eV becomes apparent, while for $E_e = 32.17$ eV, the calculations at equilibrium geometry are getting better again compared with experimental data. This suggests that the observed asymmetry in the MFPADs could be linked to the asymmetric geometry, but also influenced by the particular photon energies, thereby indicating the influence of the resonance effect.

By considering the energy shift of the Σ_u shape resonant peak and taking into account fixed-nuclei cross sections averaged over asymmetric stretch and bending modes, Miyabe [16] obtained relatively good agreement with experimental data. The same problem is encountered in the present

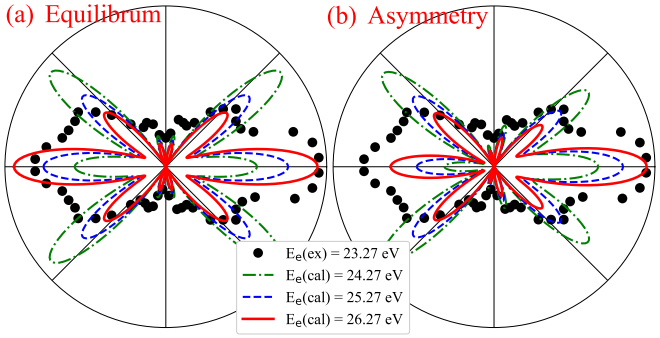

FIG. 5. Polar plots of C 1s MFPADs of CO_2 with molecular orientation parallel to the $\hat{\boldsymbol{e}}$ vector. The dots correspond to measurements reported in Ref. [50] at $E_e = 23.27$ eV. Solid red, dashed blue, and dash-dotted green curves are present calculations at $E_e = 24.27$, 25.27, and 26.27 eV, respectively. (a) Calculations at equilibrium geometry; (b) calculations at asymmetric geometry. (CO distances are 1.136 and 1.193 Å, respectively.)

calculations. Figure 5 shows the comparison between experimental data [50] measured at $E_e = 23.27$ eV and present calculations with energies shifts to $E_e = 24.27$, 25.27, and 26.27 eV. The experimental data is normalized to the calculation at $E_e = 26.27$ eV with the best visual fit. Apparently, calculations with asymmetric geometry achieve a better agreement with experimental data. With the increasing of photoelectron energies from $E_e = 24.27$ to 26.27 eV, the agreements between experiment and calculations become better. It also reflects that the shift of the shape resonant peak is ∼3 eV for the present approach, the same as the complex Kohn method [16]. The resonant peak shift of calculations can be attributed to the incomplete multicenter model potential, in which the continuum state of a photoelectron is obtained.

Figure 6 depicts the polar plots of MFPADs corresponding to C 1s photoelectrons emitted from CO_2 molecules at electron energies of $E_e = 50$, 100, and 150 eV. The molecular axis, aligned along the z axis, serves as the reference for the photon polarization directions considered in this study, namely, $\gamma_0 = 0^\circ$ ($\hat{\boldsymbol{e}} \parallel \boldsymbol{z}$), 45°, and 90° ($\hat{\boldsymbol{e}} \perp \boldsymbol{z}$), represented respectively in the first, second, and third columns. In the plot, the solid red and dashed blue lines denote calculations conducted under the dipole approximation in the length and velocity forms, respectively. The dotted orange line incorporates the nondipole effect. Notably, small deviations between the calculations in the length and velocity forms are observable. The nondipole effect in the present work exhibits negligible contribution to the cross sections within the current geometric configuration, wherein the emitted photoelectron and the molecular axis lie within the plane orthogonal to the propagation direction of incident photons. The figure does not include multiple-scattering x-ray photoelectron diffraction (XPD) calculations utilizing muffin-tin approximation theory, as presented by Kazama *et al*. [52]. Nevertheless, upon comparison, the lobular and nodal structures of the MFPADs align with our calculations, albeit with minor differences in lobe magnitudes. Despite these slight variations, the results exhibit satisfactory agreement, underscoring the validity of our present model.

It must be noted that there are still some small discrepancies if one closely investigates on the detailed distributions when comparing the present calculations with the density-functional [50] and multiple-scattering XPD [52] theories. The discrepancies can be ascribed to the adoption of a different incomplete multicenter model potential when solving the coupled-channel radial Schrödinger equation, and thus may lead to the insufficient description of the correlations between the continuum electron and residual ion, especially in the short-range region. It is a strenuous problem when encountering with the electron continuum state for the model-potential-dependent approach, especially for the multicenter molecular target. As far as we are concerned, theories of complex Kohn [15,17] and XCHEM [24] methods were proposed to address this issue, and often without corrections. However, discrepancies between calculations and experimental data still exist in the literature. It also reflects that accurately describing the ionization continuum state is a very difficult task. The advantage of the present multicenter continuum-state approach to MFPAD is that it is easier to extend to more complex polyelectronic atoms and molecules with sufficient accuracy. Based on this point, the molecular vibrational degrees of freedom can also be taken into account straightforwardly without high theoretical and technical barriers.

B. Twisted photons

Firstly, we posit a scenario wherein a macroscopic target comprising atoms or molecules is uniformly distributed across the spatial extent of the incident twisted light beam. Consequently, the differential cross sections for photoelectron emission remain unaffected by the OAM of the twisted photons. However, the resultant formula, depicted in Eq. (20), incorporates parameters pertaining to the twisted light, notably, the opening angle θ_k alongside the rotation angle ϕ_k which undergoes integration. In addition, the polarization structure of twisted light also plays an important role in determining the MFPADs. The pattern of polarization of such light has a quite complicated structure for large values of opening angle. Interesting ideas and discussions on the polarization structure complexity of twisted Bessel light can be obtained from papers [53,54]. Here, we note that the concept of linear polarization of twisted light, throughout this paper, refers to linear polarization for a specific direction of wave vector, while the overall polarization structure is not linear. In this study, two linearly polarized structures of twisted Bessel light with an opening angle θ_k are considered. One is illustrated in Fig. 7, representing a polarization cone surface, which possesses an opening angle of $90^\circ - \theta_k$, while the other is depicted in Fig. 8, representing a polarization plane.

Figures 7(b) and 7(e) and Figs. 7(c) and 7(f) illustrate the MFPADs for C 1s photoelectrons emitted from CO_2 molecules at electron energies of 50 and 100 eV, respectively, upon interaction with twisted Bessel light. As depicted in the kinematic configurations outlined in Figs. 7(a) and 7(d), the molecular axis aligns with the z axis, while photoelectron detection occurs within the xz plane. The linearly polarized vector lies within a polarization cone surface, indicated by purple lines. The various line styles in Figs. 7(b), 7(c), 7(e), and 7(f) denote distinct opening angles θ_k of the twisted Bessel beams (solid black line: $\theta_k = 0^\circ$; dash-dot

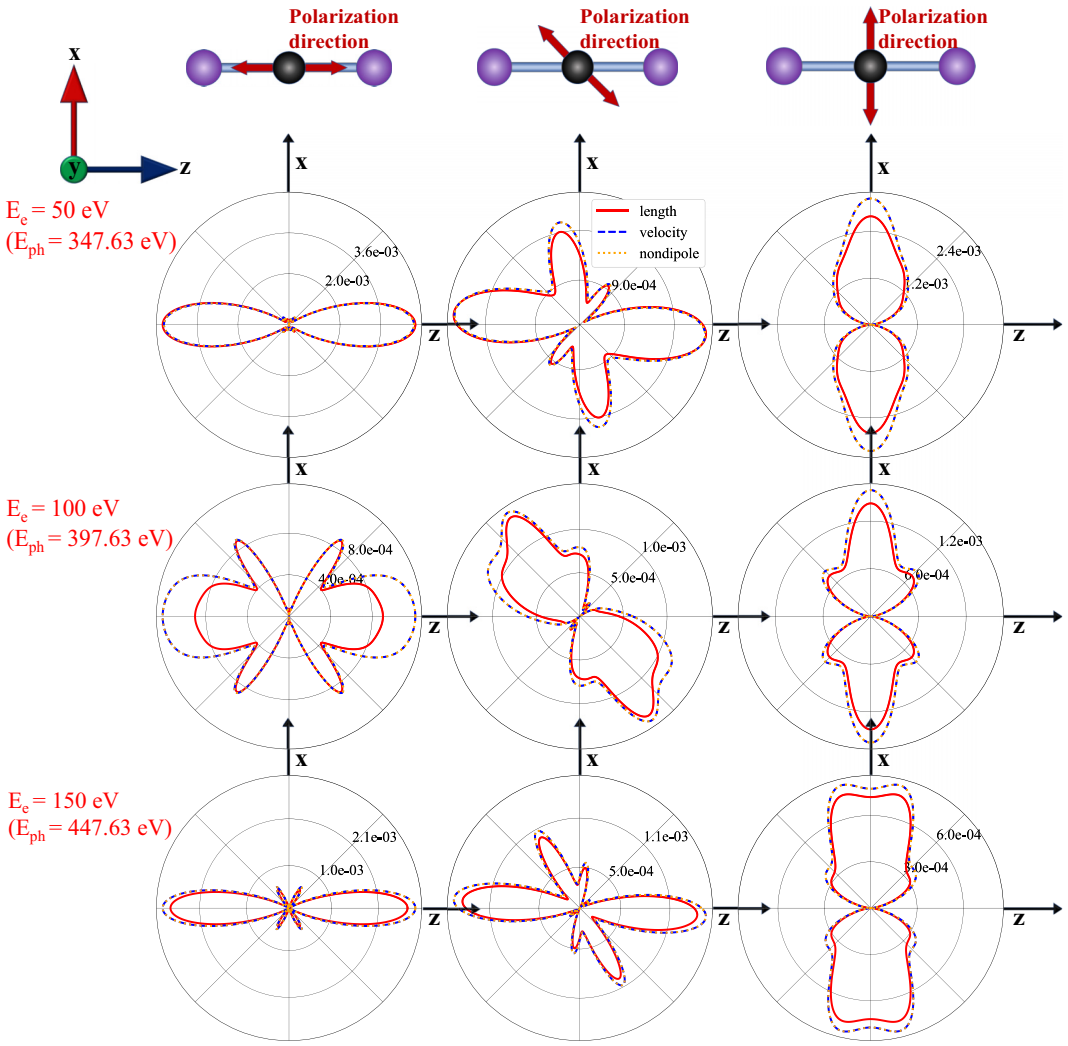

FIG. 6. Polar plots of MFPADs for C 1s photoelectrons from CO_2 molecules at $E_e = 50$, 100, and 150 eV, with the photon energy E_{ph} in the bracket. Both the polarization vector and molecular axis lie in the xz plane, and the photons propagate along the y axis, as shown in Fig. 1. γ_0 is defined as the angle between molecular orientation and polarization of photons. The first, second, and third columns display the MFPADs for γ_0 equal to 0°, 45°, and 90°, respectively. The solid red and dashed blue lines indicate present calculations under dipole approximation in the length and velocity forms, respectively. The dotted orange line is the present calculation including the nondipole effect. The results are in good agreement with previous XPD calculations (not shown) [52].

orange line: $\theta_k = 10°$; dashed blue line: $\theta_k = 20°$; solid red line: $\theta_k = 30°$).

In Fig. 7(a), the propagation direction of twisted Bessel light aligns with the z axis. When $\theta_k = 0°$, the twisted Bessel light reverts to a plane wave. Consequently, the polarization vector $\boldsymbol{e}_{k\lambda}$ lies within the xy plane, resulting in zero intensity for photoelectrons emitted at $\theta_e = 0°$ and 180°, satisfying the orthogonality condition $\boldsymbol{k}_e \perp \boldsymbol{e}_{k\lambda}$. In Figs. 7(b) and 7(c), as θ_k increases from 0° to 30°, the intensity of emitted photoelectrons at $\theta_e = 0°$ and 180° gradually rises. This trend is more pronounced for photoelectron energies at $E_e = 50$ eV. The polarization vector of twisted light exhibits a nonzero z component in the directions of $\theta_e = 0°$ and 180°. With a larger opening angle, the projection of the polarization vector of twisted light increases, leading to a higher probability of photoelectron emission at $\theta_e = 0°$ and 180°.

Consider another kinematic condition, where the propagation direction of twisted Bessel light aligns with the y axis, as the illustrated kinematics in Fig. 7(d), akin to the setup depicted in Fig. 6. In Figs. 7(e) and 7(f), the MFPADs are presented for various opening angles $\theta_k = 0°$, 10°, 20°, and 30°. Although for $\theta_k = 0°$ the twisted light reverts to a plane wave, the MFPADs in Fig. 7 do not align with any of the distributions in Fig. 6. This difference arises from the random distribution of the polarization vector directions within the xz plane for twisted light ionization. The cross sections for feasible polarization directions are integrated in practical calculations. As the opening angle increases from $\theta_k = 0°$ to 30°, the absolute value of the cross section gradually increases [dominated by $1/\cos\theta_k$ in Eq. (20)], while the shapes of MFPADs remain nearly identical. Notably, even at $\theta_k = 1°$, this trend persists (not shown).

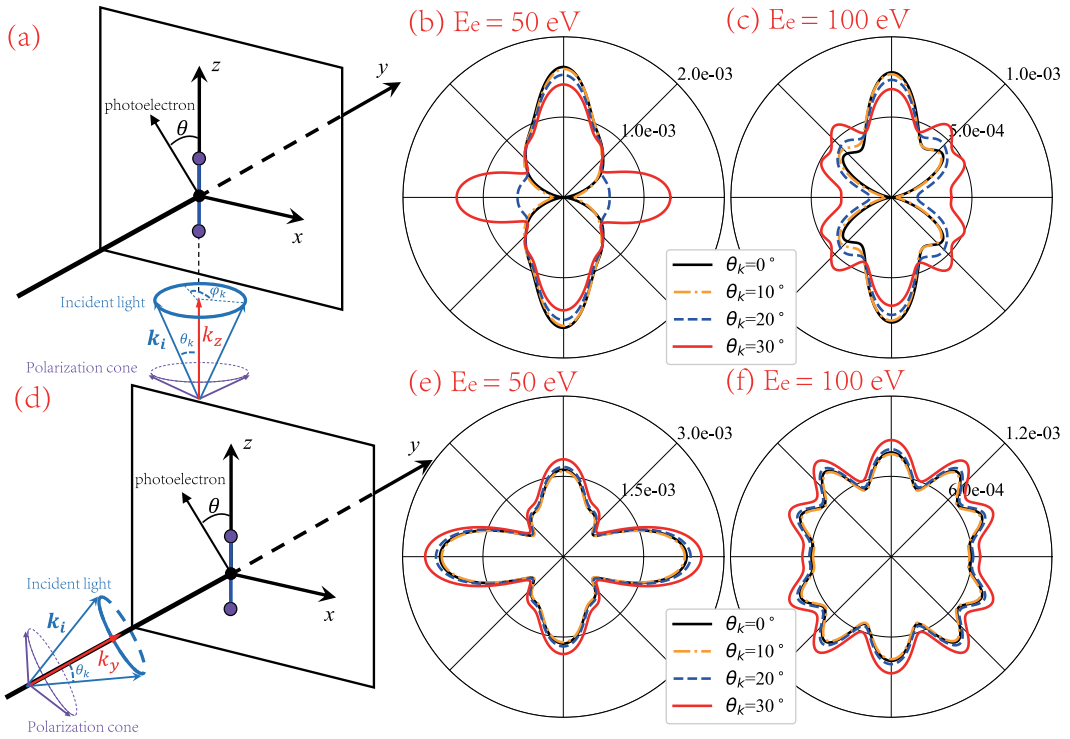

FIG. 7. Polar plots of MFPADs for C 1s photoelectrons from CO_2 molecules at $E_e = 50$ and 100 eV, induced by twisted Bessel light, with polarized vectors lying on a cone surface. As shown in Figs. 7(a) and 7(d), the photoelectron is detected in the xz plane, and the propagation direction of twisted Bessel light is along the z and y axis for the first and second row, respectively. The different types of lines indicate the different opening angle θ_k of twisted Bessel photons in (b), (c), (e), and (f). (Solid black line: $\theta_k = 0°$; dash-dot orange line: $\theta_k = 10°$; dashed blue line: $\theta_k = 20°$; solid red line: $\theta_k = 30°$).

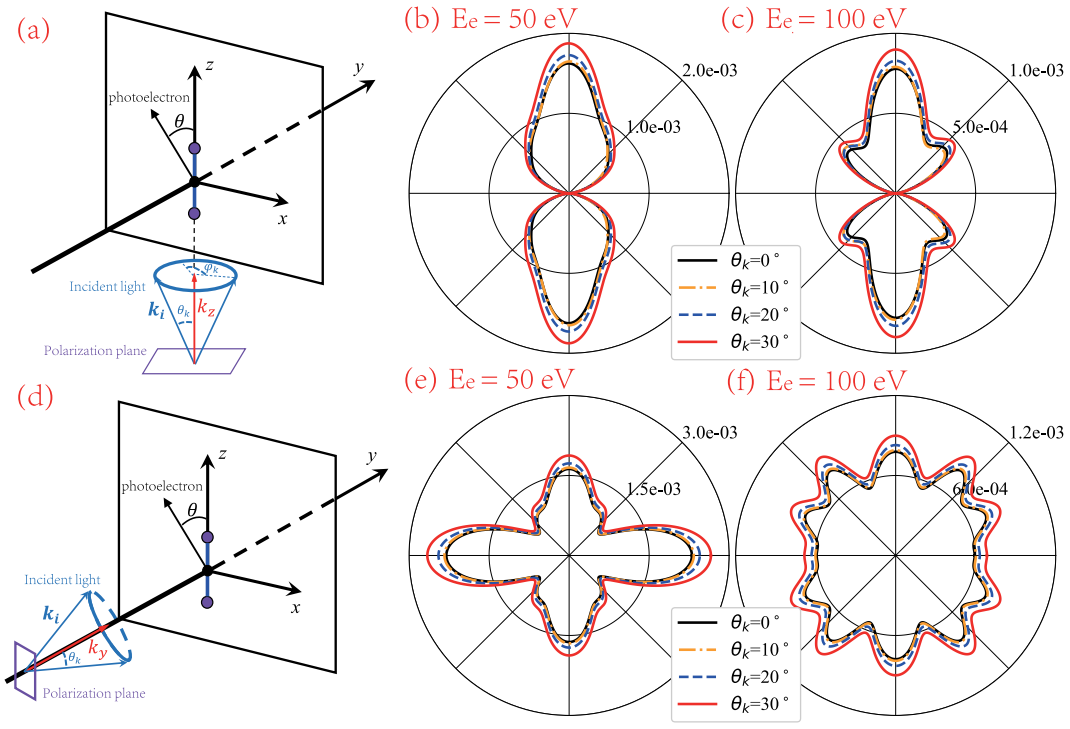

FIG. 8. Same as Fig. 7, except that the polarization vector lies at the perpendicular plane with respect to twisted light propagation.

It must be noted that the polarization structure of twisted light also plays an important role in determining the MFPADs, as mentioned before. Here, we present MFPADs resulting from twisted Bessel light similar to Fig. 7, but with a special polarization structure of twisted light. As shown in Figs. 8(a) and 8(d), the linearly polarized vector of twisted light lies in the perpendicular plane with respect to the twisted light propagation direction. Different from the results in Fig. 7, the shapes of MFPADs are not sensitive to both of the kinematic conditions and the opening angle of twisted light.

It can be inferred that both the kinematic conditions and the polarization structure of twisted light play pivotal roles in determining the MFPADs. In the case of the first polarization structure depicted in Fig. 7, when the propagation direction of twisted Bessel light is parallel to the molecular axis of CO_2, the MFPADs exhibit significant variations depending on the opening angle of the twisted light. Conversely, when the propagation direction of twisted Bessel light is perpendicular to the molecular axis, the shapes of MFPADs remain unaffected by the parameters of twisted Bessel light. These findings underscore the distinct characteristics of MFPADs under different kinematic conditions during the interaction of molecules with twisted photons. Regarding the second polarization structure illustrated in Fig. 8, the MFPADs' shapes demonstrate insensitivity to both kinematic conditions and the opening angle of twisted light.

When implementing restrictions on impact parameters, the OAM of twisted Bessel light becomes influential in the photoionization process. The spatial distribution of the twisted light beam within the coordinate system manifests as a ring-like structure, characterized by a node at the beam axis where a phase singularity is present. The significant spatial heterogeneity complicates the mathematical representation of the interaction between twisted light and matter, particularly in proximity to the phase singularity, rendering the conventional dipole-moment approximation inapplicable [53,55–58]. As demonstrated in practical experiments [55], the utilization of an ion trap stands as the prevalent methodology for acquiring experimental data with atoms positioned at the phase singularity. For theoretical computations, this condition can be achieved by setting $\boldsymbol{\rho} = 0$ in Eq. (15):

$$M_{fi}^{(\mathrm{tw})}(\boldsymbol{k}, \boldsymbol{\rho} = 0) = (-i)^{m_\gamma} \sqrt{\frac{\kappa}{2\pi}} \int_0^{2\pi} e^{i m_\gamma \phi_k} M_{fi}^{(\mathrm{pl})}(\boldsymbol{k}) \frac{d\phi_k}{2\pi}. \tag{35}$$

The OAM associated with twisted photons remains unalterable within the expression, as no integration is performed across the spatial extent of the incident twisted light beam. The transition amplitude prompted by twisted photons within the phase singularity can be conceptualized as a coherent superposition of plane-wave transition amplitudes, each with distinct propagation directions within the cone surface, modulated by an OAM-correlated phase $e^{i m_\gamma \phi_k}$. Consequently, the OAM of twisted light assumes a pivotal role in determining the transition amplitude of the twisted photoionization process. Subsequently, the differential cross section is derived by squaring the magnitude of Eq. (35) while utilizing the same normalization factor as Eq. (20). To attain a more quantitative comprehension of the underlying physics, the MFPADs for C 1s photoelectrons emitted from CO_2 molecules at $E_e =$ 100 eV under the influence of twisted Bessel light possessing an OAM of $m_\gamma = \pm 1$, and an opening angle $\theta_k = 10^\circ$ in proximity to the phase singularity at the twisted center, are depicted in Fig. 9. The kinematic conditions mirror those of Fig. 7(f). Within Fig. 9, the MFPADs exhibit significantly distinct shapes compared to the outcomes in Fig. 7(f). This discrepancy primarily arises from the coherent superposition of plane-wave transition amplitudes with diverse propagation directions within the cone surface, modulated by an OAM-associated phase $e^{i m_\gamma \phi_k}$. Moreover, the MFPADs for $m_\gamma = \pm 1$ display a mirror-symmetric nature, which stems from the absorption of twisted photons bearing opposite OAM values. Consequently, the MFPADs serve as a means to discern the left and right helicity of twisted photons. The phenomenon described, commonly referred to as circular dichroism for the absorption of twisted photons [59], presents a distinct mechanism when contrasted with the circular dichroism [60,61] observed in circularly polarized plane-wave light, a topic extensively studied over numerous years. The circular dichroism pertaining to the absorption of twisted photons garners significant interest due to the additional OAM inherent in twisted photons, offering a promising avenue for investigating the structural, electronic, and magnetic characteristics of atoms, molecules, and materials.

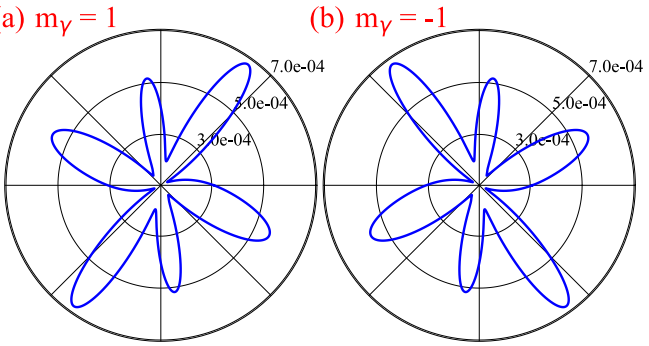

FIG. 9. Polar plots of MFPADs for C 1s photoelectrons from CO_2 molecules at $E_e = 100$ eV, induced by twisted Bessel light with orbital angular momentum of (a) $m_\gamma = 1$ and (b) $m_\gamma = -1$ in the phase singularity in the twisted center. The kinematic condition is the same as Fig. 7(d), the photoelectron is detected in the xz plane, and the propagation direction of twisted Bessel light is along the y axis. The opening angle of twisted Bessel photons is $\theta_k = 10^\circ$.

IV. SUMMARY

In the present work, we have developed a multicenter continuum-state approach uses the single-center expansion technique to describe the ionization continuum. By solving the coupled-channel Schrödinger equation in the multicenter model potential using an improved log-derivative method, the electron correlation of continuum electrons with residual ions is included through the entire interaction region. This approach enables the computation of MFPADs induced by both plane-wave and twisted photons. This approach to MFPAD can be straightforwardly extended to more complex polyelectronic atoms and molecules with sufficient accuracy. Therefore, it is expected to act as a different approach to compute MFPADs.

For the plane-wave photons, as a demonstration, the MFPADs for CO_2 1s photoelectron emission in the energy range of several to 150 eV are presented. The calculations achieve favorable agreement with experimental data and established theoretical models, indicating the validity of the present model. In addition, the asymmetry of MFPAD observed in the experimental data is also confirmed through the calculations under asymmetric geometry by considering the resonant energy peak shifts.

For the twisted photons, the MFPADs demonstrate independence from the OAM of the twisted light, provided no restrictions are imposed on the impact parameters. This observation underscores the significance of both the kinematic conditions and the polarization structure of twisted light in determining MFPADs. The investigation explores two distinct polarization structures of twisted Bessel light to elucidate MFPADs. Specifically, when considering linearly polarized vectors lying within the cone surface, characterized by an opening angle of $90^\circ - \theta_k$, the MFPAD exhibits varying dependence on the opening angle with respect to different propagation directions of twisted photons. However, when the linearly polarized vectors lie in the plane perpendicular to the propagation direction, the discernible characteristics diminish.

Additionally, for a comprehensive comprehension of the OAM-dependent photoionization process, we investigate the MFPADs resulting from placing the molecule at the phase singularity in the twisted center. The MFPADs for $m_\gamma = \pm 1$ display a mirror-symmetric nature, which stems from the absorption of twisted photons bearing opposite OAM values. The phenomenon, commonly referred to as circular dichroism for the absorption of twisted photons, presents a distinct mechanism when contrasted with the circular dichroism observed in circularly polarized plane-wave light, offering a promising avenue for investigating the structural, electronic, and magnetic characteristics of atoms, molecules, and materials.

ACKNOWLEDGMENTS

We are grateful to Dr. Xingyu Li from the University of Science and Technology of China for the fruitful discussions and the coding of the improved log-derivative method. Grants from the Fundamental Research Funds for the Central Universities (Grant No. GK202304006) and the National Natural Science Foundation of China (Grants No. 11934004, No. 12374238, and No. 11974230) are acknowledged.

APPENDIX A: IMPROVED LOG-DERIVATIVE METHOD

In order to solve the coupled equations [Eq. (27)], we employ an improved log-derivative method developed by Manolopoulos [47]. Here, we only outline the basic ideas of the method. Equation (27) can be rewritten to the following Matrix form:

$$\Phi''(r) = W(r)\Phi(r), \tag{A1}$$

in which

$$\begin{aligned}\Phi_{h\ell;h'\ell'}(r) &= f^{p\mu}_{h\ell;h'\ell'}(r)\\ W_{h\ell;h'\ell'}(r) &= U^{p\mu}_{h\ell;h'\ell'}(r) + \frac{\ell(\ell+1)}{r^2} - k_e^2.\end{aligned} \tag{A2}$$

The superscript $p\mu$ is omitted. The improved log-derivative method directly solves the following log-derivative matrix rather than the wave function and its derivative:

$$\mathbb{Y}(r) = \Phi'(r)\Phi^{-1}(r). \tag{A3}$$

Taking the derivative of the equation and utilizing Eq. (A1) will give rise to

$$\mathbb{Y}'(r) = W(r) - \mathbb{Y}^2(r). \tag{A4}$$

Matrix $\mathbb{Y}(r)$ is symmetrically inherited from the symmetric $W(r)$. In order to solve Eq. (A4), Manolopoulos defined a propagator at interval $[r', r'']$ based on the invariant imbedding principle:

$$\begin{pmatrix} \Phi'(r') \\ \Phi'(r'') \end{pmatrix} = \begin{pmatrix} \mathcal{Y}_1(r', r'') & \mathcal{Y}_2(r', r'') \\ \mathcal{Y}_3(r', r'') & \mathcal{Y}_4(r', r'') \end{pmatrix} \begin{pmatrix} -\Phi(r') \\ \Phi(r'') \end{pmatrix}. \tag{A5}$$

Then, the recurrence relation of matrix $\mathbb{Y}(r)$ satisfies

$$\begin{aligned}\mathbb{Y}(r'') = \mathcal{Y}_4(r', r'') - \mathcal{Y}_3(r', r'')[\mathbb{Y}(r') - \mathcal{Y}_1(r', r'')]^{-1}\\ \times\ \mathcal{Y}_2(r', r'').\end{aligned} \tag{A6}$$

From the asymptotic boundary conditions of Eq. (28),

$$\mathbb{Y}(r \to 0)_{h\ell;h'\ell'} = (\ell+1)r^{-1}\delta_{h\ell;h''\ell''}. \tag{A7}$$

Combining the asymptotic boundary condition and the recurrence relation, $\mathbb{Y}(r)$ can be obtained at arbitrary r using the propagator.

In the original Manolopoulos improved log-derivative method [47], the propagation sector $[a, b]$ is uniformly divided to two half-sectors, $[a, c]$ and $[c, b]$ with $c - a = b - c = h$. In the following expressions, $[r', r'']$ denotes both $[a, c]$ and $[c, b]$ intervals. And, a piecewise constant diagonal reference potential is adopted:

$$W_{\text{ref}}(r)_{ij} = \delta_{ij}p_j^2,\ r \in [a, b]; \tag{A8}$$

with this analytical reference potential, the homogeneous equation

$$\Phi''(r) = W_{\text{ref}}(r)\Phi(r) \tag{A9}$$

is easily solved analytically. Then, the corresponding propagator for the half-sector $[r', r'']$ is also easily obtained:

$$\begin{aligned} y_1(r', r'')_{ij} = y_4(r', r'')_{ij} &= \delta_{ij}\begin{cases} |p_j|\coth|p_j|h, & p_j^2 \geqslant 0 \\ |p_j|\cot|p_j|h, & p_j^2 \leqslant 0 \end{cases}\\ y_2(r', r'')_{ij} = y_3(r', r'')_{ij} &= \delta_{ij}\begin{cases} |p_j|\operatorname{csch}|p_j|h, & p_j^2 \geqslant 0 \\ |p_j|\csc|p_j|h, & p_j^2 \leqslant 0 \end{cases}. \end{aligned} \tag{A10}$$

For the complete potential, the propagator is related to the above analytical reference propagator:

$$\begin{aligned}\mathcal{Y}_1(r', r'') &= y_1(r', r'') + Q(r'),\\ \mathcal{Y}_2(r', r'') &= y_2(r', r''),\\ \mathcal{Y}_3(r', r'') &= y_3(r', r''),\\ \mathcal{Y}_4(r', r'') &= y_4(r', r'') + Q(r'').\end{aligned} \tag{A11}$$

If we define the residual coupling matrix,

$$U(r) = W(r) - W_{\text{ref}}(r), \tag{A12}$$

then the quadrature contributions from the three grid points are given by

$$\begin{aligned} Q(a) &= \frac{h}{3}U(a), \\ Q(c) &= \frac{4}{h}\left[I - \frac{h^2}{6}U(c)\right]^{-1} - \frac{4}{h}I, \\ Q(b) &= \frac{h}{3}U(b), \end{aligned} \tag{A13}$$

which are identical to those used in the modified Simpson's rule integration.

After the entire propagation of the log-derivative matrix, according to the following matrix form of boundary conditions,

$$\begin{aligned} \Phi(r) &= \mathbb{F}(r) + \mathbb{G}(r)\mathcal{K} \\ \Phi'(r) &= \mathbb{F}'(r) + \mathbb{G}'(r)\mathcal{K}, \end{aligned} \tag{A14}$$

the corresponding reaction $\mathcal{K}$-matrix can be extracted,

$$\mathcal{K} = -[\mathbb{Y}(r)\mathbb{G}(r) - \mathbb{G}'(r)]^{-1}[\mathbb{Y}(r)\mathbb{F}(r) - \mathbb{F}'(r)], \tag{A15}$$

where r represents the asymptotic boundary value $r_{\max}$. $\mathbb{F}(r)$ and $\mathbb{G}(r)$ are diagonal matrices, whose diagonal terms are $F(k_e r)$ and $G(k_e r)$, respectively. $\mathbb{F}'(r)$ and $\mathbb{G}'(r)$ are their derivative matrices.

APPENDIX B: NUMERICAL PROCESS FOR TRANSITION AMPLITUDE

1. Length form in dipole approximation

Except for the multicenter continuum state, the dipole transition amplitude depends on the initial bound orbital $\varphi_i(\boldsymbol{r})$, which is also expanded with the symmetry-adapted angular function:

$$\varphi_i(\boldsymbol{r}) = \frac{1}{r}\sum_{h_3\ell_3} u_{h_3\ell_3}(r) X^{i\mu}_{h_3\ell_3}(\hat{\boldsymbol{r}}). \tag{B1}$$

In addition, the dipole transition amplitude also depends on the polarization of electric field; let $\boldsymbol{e}_{\boldsymbol{k}\lambda}$ denotes the polarization vector, then the interaction can be expressed in terms of rotation operator,

$$\boldsymbol{e}_{\boldsymbol{k}\lambda}\cdot\boldsymbol{r} = \sqrt{\frac{4\pi}{3}} r \sum_{m=-1}^{1} Y_{1m}(\hat{\boldsymbol{r}}) D^1_{m\lambda}(\phi_k, \theta_k, 0). \tag{B2}$$

$D^1_{m\lambda}$ is the big Wigner rotation matrix with the Euler angles $\Omega = (\phi_k, \theta_k, 0)$, which defines the rotation from the molecular to the photon frame. $Y_{1m}(\hat{\boldsymbol{r}})$ is the spherical harmonics with $\ell = 1$. Inserting Eqs. (33) and (B1) into dipole transition amplitude,

$$\begin{aligned} &\langle \mathcal{F}^{(-)}_{\boldsymbol{k}_e}(\boldsymbol{r})|\boldsymbol{e}_{\boldsymbol{k}\lambda}\cdot\boldsymbol{r}|\varphi_i(\boldsymbol{r})\rangle \\ &= \frac{1}{(2\pi)^{\frac{3}{2}}}\sum_{p\mu}\sum_{h_1\ell_1}\sum_{h_2\ell_2}\sum_{h_3\ell_3} 4\pi i^{\ell_1} e^{-i\sigma_{\ell_1}} \frac{1}{k_e} \\ &\quad\times \int_0^\infty \sum_{h\ell} f^{p\mu}_{h_1\ell_1;h\ell}(k_e, r)([\mathcal{I} + i\mathcal{K}^{p\mu}]^{-1})^*_{h\ell;h_2\ell_2} r u_{h_3\ell_3}(r) dr \\ &\quad\times \sqrt{\frac{4\pi}{3}}\sum_m \int X^{p\mu}_{h_2\ell_2}(\hat{\boldsymbol{r}}) X^{i\mu}_{h_3\ell_3}(\hat{\boldsymbol{r}}) Y_{1m}(\hat{\boldsymbol{r}}) d\hat{\boldsymbol{r}} \\ &\quad\times D^1_{m\lambda}(\phi_k, \theta_k, 0) X^{p\mu}_{h_1\ell_1}(\hat{\boldsymbol{k}}_{\boldsymbol{e}}), \end{aligned} \tag{B3}$$

in which the spherical harmonics $Y_{1m}(\hat{\boldsymbol{r}})$ can be expressed in terms of real spherical harmonics $S_{1m}(\hat{\boldsymbol{r}})$

$$\begin{aligned} Y_{11}(\hat{\boldsymbol{r}}) &= \frac{\sqrt{2}}{2}[S_{11}(\hat{\boldsymbol{r}}) + iS_{1-1}(\hat{\boldsymbol{r}})],\ Y_{10}(\hat{\boldsymbol{r}}) = S_{10}(\hat{\boldsymbol{r}}), \\ Y_{1-1}(\hat{\boldsymbol{r}}) &= \frac{\sqrt{2}}{2}[-S_{11}(\hat{\boldsymbol{r}}) + iS_{1-1}(\hat{\boldsymbol{r}})]. \end{aligned} \tag{B4}$$

The symmetry-adapted angular function $X^{p\mu}_{h\ell}(\hat{\boldsymbol{r}})$ is defined as a linear combination of real spherical harmonics $S_{\ell m}(\hat{\boldsymbol{r}})$ [32–34],

$$X^{p\mu}_{h\ell}(\hat{\boldsymbol{r}}) = \sum_{m=-\ell}^{\ell} b^{p\mu}_{h\ell m} S_{\ell m}(\hat{\boldsymbol{r}}). \tag{B5}$$

The angular integration part in Eq. (B3) is directly related to the real GAUNT coefficient [62], determined by quantum numbers.

2. Velocity form

Here, we start from the plane-wave transition amplitude of Eq. (5) in the velocity form by including the nondipole term. For convenience, we specify a coordinate system, in which the wave vector $\boldsymbol{k}$ of the incoming photon is adopted along the quantization axis, $z \parallel \boldsymbol{k}$. As the photon polarization and wave vectors are orthogonal to each other, $\boldsymbol{e}_{\boldsymbol{k}\lambda}\cdot\boldsymbol{k} = 0$, then the transition amplitude of Eq. (5) can be expressed as

$$M^{(\mathrm{pl})}_{fi}(\theta_k = 0, \phi_k = 0) = \langle \mathcal{F}^{(-)}_{\boldsymbol{k}_e}(\boldsymbol{r})|e^{ikz}\nabla_\lambda|\varphi_i(\boldsymbol{r})\rangle, \tag{B6}$$

where ∇_λ refers to the spherical components of the nabla operator with $\lambda = \pm 1$, and λ is associated with the helicity of the incident wave.

By considering the expansion of initial wave function of Eq. (B1), a crucial step to numerically evaluate its gradient in Eq. (B6) is

$$\nabla_\lambda \varphi_i(\boldsymbol{r}) = \sum_{h_3\ell_3}\sum_{m_3} b^{i\mu}_{h_3\ell_3 m_3} \nabla_\lambda\left[\mathcal{R}_{h_3\ell_3}(r) S_{\ell_3 m_3}(\hat{\boldsymbol{r}})\right], \tag{B7}$$

where

$$\mathcal{R}_{h_3\ell_3}(r) \equiv \frac{1}{r} u_{h_3\ell_3}(r). \tag{B8}$$

By utilizing the relation between real spherical harmonics $S_{\ell m}(\hat{\boldsymbol{r}})$ and symmetry-adapted angular function $X^{p\mu}_{h\ell}(\hat{\boldsymbol{r}})$ [32–34] ($m \geqslant 0$),

$$\begin{aligned} S_{\ell m}(\hat{\boldsymbol{r}}) &= \frac{1}{\sqrt{2}}[Y_{\ell m}(\hat{\boldsymbol{r}}) + (-1)^m Y_{\ell -m}(\hat{\boldsymbol{r}})],\ S_{\ell 0}(\hat{\boldsymbol{r}}) = Y_{\ell 0}(\hat{\boldsymbol{r}}), \\ S_{\ell -m}(\hat{\boldsymbol{r}}) &= \frac{i}{\sqrt{2}}[-Y_{\ell m}(\hat{\boldsymbol{r}}) + (-1)^m Y_{\ell -m}(\hat{\boldsymbol{r}})], \end{aligned} \tag{B9}$$

the gradient of initial wave function expanded by the real spherical harmonics in Eq. (B6) can be expressed as a linear

combination of the gradient associated with complex spherical harmonics [36,63],

$$\nabla_\lambda\big[\mathcal{R}_{h_3\ell_3}(r)Y_{\ell_3 m_3}(\hat{\boldsymbol{r}})\big] = \sum_{\Lambda_i=\ell_3\pm1} A^{\lambda}_{\Lambda_i m_3}\tilde{\mathcal{R}}_{\Lambda_i}(r)Y_{\Lambda_i m_3+\lambda}(\hat{\boldsymbol{r}}), \tag{B10}$$

where

$$A^{\pm1}_{\ell_3+1m_3} = \sqrt{\frac{(\ell_3\pm m_3+1)(\ell_3\pm m_3+2)}{2(2\ell_3+1)(2\ell_3+3)}},$$
$$A^{\pm1}_{\ell_3-1m_3} = \sqrt{\frac{(\ell_3\mp m_3-1)(\ell_3\mp m_3)}{2(2\ell_3-1)(2\ell_3+1)}}. \tag{B11}$$

$$\tilde{\mathcal{R}}_{\ell_3+1}(r) = \frac{\partial\mathcal{R}_{h_3\ell_3}(r)}{\partial r} - \frac{\ell_3}{r}\mathcal{R}_{h_3\ell_3}(r),$$
$$\tilde{\mathcal{R}}_{\ell_3-1}(r) = \frac{\partial\mathcal{R}_{h_3\ell_3}(r)}{\partial r} + \frac{\ell_3+1}{r}\mathcal{R}_{h_3\ell_3}(r). \tag{B12}$$

Combining Eqs. (B7), (B9), and (B10) will give rise to a classification discussion. When $m_3 > 0$,

$$\begin{aligned}
&\nabla_\lambda[\mathcal{R}_{h_3\ell_3}(r)S_{\ell_3 m_3}(\hat{\boldsymbol{r}})]\\
&= \frac{1}{\sqrt{2}}\{\nabla_\lambda[\mathcal{R}_{h_3\ell_3}(r)Y_{\ell_3 m_3}(\hat{\boldsymbol{r}})]\\
&\quad + (-1)^{m_3}\nabla_\lambda[\mathcal{R}_{h_3\ell_3}(r)Y_{\ell_3-m_3}(\hat{\boldsymbol{r}})]\}\\
&= \frac{1}{\sqrt{2}}\sum_{\Lambda_i=\ell_3\pm1}\tilde{\mathcal{R}}_{\Lambda_i}(r)\big[A^{\lambda}_{\Lambda_i m_3}Y_{\Lambda_i m_3+\lambda}(\hat{\boldsymbol{r}})\\
&\quad + (-1)^{m_3}A^{\lambda}_{\Lambda_i-m_3}Y_{\Lambda_i-m_3+\lambda}(\hat{\boldsymbol{r}})\big];
\end{aligned} \tag{B13}$$

when $m_3 = 0$,

$$\begin{aligned}
\nabla_\lambda[\mathcal{R}_{h_3\ell_3}(r)S_{\ell_3 m_3}(\hat{\boldsymbol{r}})] &= \nabla_\lambda[\mathcal{R}_{h_3\ell_3}(r)Y_{\ell_3 m_3}(\hat{\boldsymbol{r}})]\\
&= \sum_{\Lambda_i=\ell_3\pm1} A^{\lambda}_{\Lambda_i m_3}\tilde{\mathcal{R}}_{\Lambda_i}(r)Y_{\Lambda_i m_3+\lambda}(\hat{\boldsymbol{r}});
\end{aligned} \tag{B14}$$

when $m_3 < 0$,

$$\begin{aligned}
&\nabla_\lambda[\mathcal{R}_{h_3\ell_3}(r)S_{\ell_3 m_3}(\hat{\boldsymbol{r}})]\\
&= \frac{i}{\sqrt{2}}\big\{-\nabla_\lambda\big[\mathcal{R}_{h_3\ell_3}(r)Y_{\ell_3-m_3}(\hat{\boldsymbol{r}})\big]\\
&\quad + (-1)^{m_3}\nabla_\lambda\big[\mathcal{R}_{h_3\ell_3}(r)Y_{\ell_3 m_3}(\hat{\boldsymbol{r}})\big]\big\}\\
&= \frac{i}{\sqrt{2}}\sum_{\Lambda_i=\ell_3\pm1}\tilde{\mathcal{R}}_{\Lambda_i}(r)\big[-A^{\lambda}_{\Lambda_i-m_3}Y_{\Lambda_i-m_3+\lambda}(\hat{\boldsymbol{r}})\\
&\quad + (-1)^{m_3}A^{\lambda}_{\Lambda_i m_3}Y_{\Lambda_i m_3+\lambda}(\hat{\boldsymbol{r}})\big].
\end{aligned} \tag{B15}$$

Overall, we can define

$$\nabla_\lambda\big[\mathcal{R}_{h_3\ell_3}(r)S_{\ell_3 m_3}(\hat{\boldsymbol{r}})\big] \equiv \sum_{\Lambda_i=\ell_3\pm1}\tilde{\mathcal{R}}_{\Lambda_i}(r)B^{\lambda}_{\Lambda_i m_3}(\hat{\boldsymbol{r}}), \tag{B16}$$

where

$$\begin{aligned}
B^{\lambda}_{\Lambda_i m_3}(\hat{\boldsymbol{r}}) &= \frac{1}{\sqrt{2}}\big[A^{\lambda}_{\Lambda_i m_3}Y_{\Lambda_i m_3+\lambda}(\hat{\boldsymbol{r}})\\
&\quad + (-1)^{m_3}A^{\lambda}_{\Lambda_i-m_3}Y_{\Lambda_i-m_3+\lambda}(\hat{\boldsymbol{r}})\big], m_3 > 0\\
&= A^{\lambda}_{\Lambda_i m_3}Y_{\Lambda_i m_3+\lambda}(\hat{\boldsymbol{r}}), m_3 = 0\\
&= \frac{i}{\sqrt{2}}\big[-A^{\lambda}_{\Lambda_i-m_3}Y_{\Lambda_i-m_3+\lambda}(\hat{\boldsymbol{r}})\\
&\quad + (-1)^{m_3}A^{\lambda}_{\Lambda_i m_3}Y_{\Lambda_i m_3+\lambda}(\hat{\boldsymbol{r}})\big], m_3 < 0.
\end{aligned} \tag{B17}$$

Finally, the gradient of the bound state can be expressed in a brief form:

$$\nabla_\lambda\varphi_i(\boldsymbol{r}) = \sum_{h_3\ell_3}\sum_{m_3} b^{i\mu}_{h_3\ell_3 m_3}\sum_{\Lambda_i=\ell_3\pm1}\tilde{\mathcal{R}}_{\Lambda_i}(r)B^{\lambda}_{\Lambda_i m_3}(\hat{\boldsymbol{r}}). \tag{B18}$$

We can rotate the vector $\boldsymbol{k}$ to an arbitrary direction $\hat{\boldsymbol{k}} = \boldsymbol{k}/k = (\theta_k, \phi_k)$ by a rotation of the initial bound and multicenter continuum states through a matrix, which acts on the real spherical harmonics $R^{\ell}_{m'm}$ [64],

$$S_{\ell m}(\hat{\boldsymbol{r}}) = \sum_{m'} S_{\ell m'}(\hat{\boldsymbol{r}}')R^{\ell}_{m'm}(\phi_k, \theta_k, 0). \tag{B19}$$

Considering the following expansion,

$$e^{ikz} = \sqrt{4\pi}\sum_{\ell_4} i^{\ell_4}\sqrt{2\ell_4+1}\, j_{\ell_4}(kr)S_{\ell_4 0}(\hat{\boldsymbol{r}}), \tag{B20}$$

and combining Eqs. (B1), (33), and (B19), after simplification, the transition amplitude of Eq. (5) with an arbitrary direction of wave vector $\hat{\boldsymbol{k}} = (\theta_k, \phi_k)$ can be expressed as

$$\begin{aligned}
M^{(\mathrm{pl})}_{fi}(\boldsymbol{k}) &= \frac{4}{k_e}\sum_{p\mu}\sum_{h_1\ell_1} i^{-\ell_1}e^{i\sigma_{\ell_1}}X^{p\mu}_{h_1\ell_1}(\hat{\boldsymbol{k}}_e)\\
&\quad\times\sum_{h_2\ell_2}\sum_{h_3\ell_3}\sum_{\Lambda_i=\ell_3\pm1}\sum_{\ell_4} i^{\ell_4}\sqrt{2\ell_4+1}\\
&\quad\times\int\phi^{p\mu}_{h_1\ell_1;h_2\ell_2}(k_e, r)j_{\ell_4}(kr)\tilde{\mathcal{R}}_{\Lambda_i}(r)rdr\\
&\quad\times\sum_{m_2} b^{p\mu}_{h_2\ell_2 m_2}\sum_{m_3} b^{i\mu}_{h_3\ell_3 m_3}\\
&\quad\times\sum_{m'_2,m'_3} R^{\ell_2}_{m'_2 m_2}(\phi_k, \theta_k, 0)R^{\ell_3}_{m'_3 m_3}(\phi_k, \theta_k, 0)\\
&\quad\times\int S_{\ell_2 m'_2}(\hat{\boldsymbol{r}})S_{\ell_4 0}(\hat{\boldsymbol{r}})B^{\lambda}_{\Lambda_i m'_3}(\hat{\boldsymbol{r}})d\boldsymbol{r}.
\end{aligned} \tag{B21}$$

[1] B. W. J. McNeil and N. R. Thompson, Nat. Photon. **4**, 814 (2010).

[2] P. Emma, R. Akre, J. Arthur, R. Bionta, C. Bostedt, J. Bozek, A. Brachmann, P. Bucksbaum, R. Coffee, F.-J. Decker, Y. Ding, D. Dowell, S. Edstrom, A. Fisher, J. Frisch, S. Gilevich, J. Hastings, G. Hays, Ph. Hering, Z. Huang *et al.*, Nat. Photon. **4**, 641 (2010).

[3] C. Pellegrini, A. Marinelli, and S. Reiche, Rev. Mod. Phys. **88**, 015006 (2016).

[4] E. A. Seddon, J. A. Clarke, D. J. Dunning, C. Masciovecchio, C. J. Milne, F. Parmigiani, D. Rugg, J. C. H. Spence, N. R. Thompson, K. Ueda, S. M. Vinko, J. S. Wark, and W. Wurth, Rep. Prog. Phys. **80**, 115901 (2017).

[5] M. P. Minitti, J. M. Budarz, A. Kirrander, J. S. Robinson, D. Ratner, T. J. Lane, D. Zhu, J. M. Glownia, M. Kozina, H. T. Lemke, M. Sikorski, Y. Feng, S. Nelson, K. Saita, B. Stankus, T. Northey, J. B. Hastings, and P. M. Weber, Phys. Rev. Lett. **114**, 255501 (2015).

[6] T. J. A. Wolf, D. M. Sanchez, J. Yang, R. M. Parrish, J. P. F. Nunes, M. Centurion, R. Coffee, J. P. Cryan, M. Gühr, K. Hegazy, A. Kirrander, R. K. Li, J. Ruddock, X. Shen, T. Vecchione, S. P. Weathersby, P. M. Weber, K. Wilkin, H. Yong, Q. Zheng *et al.*, Nat. Chem. **11**, 504 (2019).

[7] J. J. Larsen, K. Hald, N. Bjerre, H. Stapelfeldt, and T. Seideman, Phys. Rev. Lett. **85**, 2470 (2000).

[8] I. Vela-Peréz, F. Ota, A. Mhamdi, Y. Tamura, J. Rist, N. Melzer, S. Uerken, G. Nalin, N. Anders, D. You, M. Kircher, C. Janke, M. Waitz, F. Trinter, R. Guillemin, M. N. Piancastelli, M. Simon, V. T. Davis, J. B. Williams, R. Dörner *et al.*, Phys. Chem. Chem. Phys. **25**, 13784 (2023).

[9] R. Dörner, V. Mergel, O. Jagutzki, L. Spielberger, J. Ullrich, R. Moshammer, and H. Schmidt-Böcking, Phys. Rep. **330**, 95 (2000).

[10] A. Landers, T. Weber, I. Ali, A. Cassimi, M. Hattass, O. Jagutzki, A. Nauert, T. Osipov, A. Staudte, M. H. Prior, H. Schmidt-Böcking, C. L. Cocke, and R. Dörner, Phys. Rev. Lett. **87**, 013002 (2001).

[11] D. Dill and J. L. Dehmer, J. Chem. Phys. **61**, 692 (1974).

[12] D. Dill, J. Siegel, and J. L. Dehmer, J. Chem. Phys. **65**, 3158 (1976).

[13] L. Moore, M. Lysaght, L. Nikolopoulos, J. Parker, H. van der Hart, and K. Taylor, J. Mod. Opt. **58**, 1132 (2011).

[14] J. M. Carr, P. G. Galiatsatos, J. D. Gorfinkiel, A. G. Harvey, M. A. Lysaght, D. Madden, Z. Mašín, M. Plummer, J. Tennyson, and H. N. Varambhia, Eur. Phys. J. D **66**, 58 (2012).

[15] T. N. Rescigno, B. H. Lengsfield, III, A. E. Orel, J. Chem. Phys. **99**, 5097 (1993).

[16] S. Miyabe, C. W. McCurdy, A. E. Orel, and T. N. Rescigno, Phys. Rev. A **79**, 053401 (2009).

[17] C. S. Trevisan, C. W. McCurdy, and T. N. Rescigno, J. Phys. B: At. Mol. Opt. Phys. **45**, 194002 (2012).

[18] T. Fujikawa and H. Arai, J. Electron Spectrosc. Relat. Phenom. **123**, 19 (2002).

[19] F. A. Gianturco, R. R. Lucchese, and N. Sanna, J. Chem. Phys. **100**, 6464 (1994).

[20] A. P. P. Natalense and R. R. Lucchese, J. Chem. Phys. **111**, 5344 (1999).

[21] R. R. Lucchese, K. Takatsuka, and V. McKoy, Phys. Rep. **131**, 147 (1986).

[22] R. E. Stratmann and R. R. Lucchese, J. Chem. Phys. **102**, 8493 (1995).

[23] R. R. Lucchese, A. Lafosse, J. C. Brenot, P. M. Guyon, J. C. Houver, M. Lebech, G. Raseev, and D. Dowek, Phys. Rev. A **65**, 020702(R) (2002).

[24] C. Marante, M. Klinker, I. Corral, J. González-Vázquez, L. Argenti, and F. Martín, J. Chem. Theory Comput. **13**, 499 (2017).

[25] C. Marante, M. Klinker, T. Kjellsson, E. Lindroth, J. González-Vázquez, L. Argenti, and F. Martín, Phys. Rev. A **96**, 022507 (2017).

[26] M. Klinker, C. Marante, L. Argenti, J. González-Vázquez, and F. Martín, J. Phys. Chem. Lett. **9**, 756 (2018).

[27] V. J. Borrás, J. González-Vázquez, L. Argenti, and F. Martín, J. Chem. Theory Comput. **17**, 6330 (2021).

[28] P. Fernández-Milán, V. J. Borrás, J. González-Vázquez, and F. Martín, J. Chem. Phys. **158**, 134305 (2023).

[29] O. Matula, A. G. Hayrapetyan, V. G. Serbo, A. Surzhykov, and S. Fritzsche, J. Phys. B: At. Mol. Opt. Phys. **46**, 205002 (2013).

[30] A. A. Peshkov, S. Fritzsche, and A. Surzhykov, Phys. Rev. A **92**, 043415 (2015).

[31] M. D. Kiselev, E. V. Gryzlova, and A. N. Grum-Grzhimailo, Phys. Rev. A **108**, 023117 (2023).

[32] N. Sanna and F. Gianturco, Comput. Phys. Commun. **128**, 139 (2000).

[33] N. Sanna and G. Morelli, Comput. Phys. Commun. **162**, 51 (2004).

[34] N. Sanna, I. Baccarelli, and G. Morelli, Comput. Phys. Commun. **180**, 2544 (2009).

[35] J. W. Cooper, Phys. Rev. A **47**, 1841 (1993).

[36] H. M. Scholz-Marggraf, S. Fritzsche, V. G. Serbo, A. Afanasev, and A. Surzhykov, Phys. Rev. A **90**, 013425 (2014).

[37] S. Tsuru, T. Fujikawa, M. Stener, P. Decleva, and A. Yagishita, J. Chem. Phys. **148**, 124101 (2018).

[38] M. J. Frisch *et al.*, *Gaussian 09, Revision A.02*, Tech. Rep. (Gaussian, Inc., Wallingford CT, 2009).

[39] A. D. Becke, J. Chem. Phys. **98**, 5648 (1993).

[40] C. Lee, W. Yang, and R. G. Parr, Phys. Rev. B **37**, 785 (1988).

[41] T. H. D., Jr., J. Chem. Phys. **90**, 1007 (1989).

[42] I. P. Ivanov and V. G. Serbo, Phys. Rev. A **84**, 033804 (2011).

[43] M. Gong, Y. Cheng, S. B. Zhang, and X. Chen, Phys. Rev. A **106**, 012818 (2022).

[44] V. Serbo, I. P. Ivanov, S. Fritzsche, D. Seipt, and A. Surzhykov, Phys. Rev. A **92**, 012705 (2015).

[45] S. B. Zhang, X. Y. Li, J. G. Wang, Y. Z. Qu, and X. Chen, Phys. Rev. A **89**, 052711 (2014).

[46] M. Gong, X. Li, S. B. Zhang, S. Niu, X. Ren, E. Wang, A. Dorn, and X. Chen, Phys. Rev. A **98**, 042710 (2018).

[47] D. E. Manolopoulos, J. Chem. Phys. **85**, 6425 (1986).

[48] P. G. Burke, *R-Matrix Theory of Atomic Collisions*, Springer Series on Atomic, Optical and Plasma Physics, Vol. 61 (Springer, Berlin, 2011).

[49] K. C. Prince, L. Avaldi, M. Coreno, R. Camilloni, and M. de Simone, J. Phys. B: At. Mol. Opt. Phys. **32**, 2551 (1999).

[50] X.-J. Liu, H. Fukuzawa, T. Teranishi, A. De Fanis, M. Takahashi, H. Yoshida, A. Cassimi, A. Czasch, L. Schmidt, R. Dörner, K. Wang, B. Zimmermann, V. McKoy, I. Koyano, N. Saito, and K. Ueda, Phys. Rev. Lett. **101**, 083001 (2008).

[51] N. Saito, A. D. Fanis, K. Kubozuka, M. Machida, M. Takahashi, H. Yoshida, I. H. Suzuki, A. Cassimi, A. Czasch, L. Schmidt, R.

Dörner, K. Wang, B. Zimmermann, V. McKoy, I. Koyano, and K. Ueda, J. Phys. B: At. Mol. Opt. Phys. **36**, L25 (2003).

[52] M. Kazama, H. Shinotsuka, T. Fujikawa, M. Stener, P. Decleva, J. ichi Adachi, T. Mizuno, and A. Yagishita, J. Electron Spectrosc. Relat. Phenom. **185**, 535 (2012).

[53] G. F. Quinteiro, D. E. Reiter, and T. Kuhn, Phys. Rev. A **91**, 033808 (2015).

[54] D. Sarenac, J. Nsofini, I. Hincks, M. Arif, C. W. Clark, D. G. Cory, M. G. Huber, and D. A. Pushin, New J. Phys. **20**, 103012 (2018).

[55] C. T. Schmiegelow, J. Schulz, H. Kaufmann, T. Ruster, U. G. Poschinger, and F. Schmidt-Kaler, Nat. Commun. **7**, 12998 (2016).

[56] G. F. Quinteiro, D. E. Reiter, and T. Kuhn, Phys. Rev. A **95**, 012106 (2017).

[57] O. V. Angelsky, A. Y. Bekshaev, M. V. Vasnetsov, C. Y. Zenkova, P. P. Maksimyak, and J. Zheng, Front. Phys. **10**, (2022).

[58] A. Alharbi, A. Lyras, V. E. Lembessis, and O. Al-Dossary, Results Phys. **46**, 106311 (2023).

[59] G. De Ninno, J. Wätzel, P. R. Ribič, E. Allaria, M. Coreno, M. B. Danailov, C. David, A. Demidovich, M. Di Fraia, L. Giannessi, K. Hansen, Š. Krušič, M. Manfredda, M. Meyer, A. Mihelič, N. Mirian, O. Plekan, B. Ressel, B. Rösner, A. Simoncig *et al.*, Nat. Photonics **14**, 554 (2020).

[60] T. Jahnke, Th. Weber, A. L. Landers, A. Knapp, S. Schössler, J. Nickles, S. Kammer, O. Jagutzki, L. Schmidt, A. Czasch, T. Osipov, E. Arenholz, A. T. Young, R. D. Muiño, D. Rolles, F. J. G. de Abajo, C. S. Fadley, M. A. Van Hove, S. K. Semenov, N. A. Cherepkov *et al.*, Phys. Rev. Lett. **88**, 073002 (2002).

[61] D. Dowek, J. F. Pérez-Torres, Y. J. Picard, P. Billaud, C. Elkharrat, J. C. Houver, J. L. Sanz-Vicario, and F. Martín, Phys. Rev. Lett. **104**, 233003 (2010).

[62] H. H. Homeier and E. Steinborn, J. Mol. Struct.: THEOCHEM **368**, 31 (1996).

[63] D. A. Varshalovich, A. N. Moskalev, and V. K. Khersonskii, *Quantum Theory of Angular Momentum* (World Scientific, Singapore, 1988).

[64] J. Álvarez Collado, J. F. Rico, R. López, M. Paniagua, and G. Ramírez, Comput. Phys. Commun. **52**, 323 (1989).